Journal of Applied Physics ARTICLE scitation.org/journal/jap

Theoretical study of strain induced magnetic transition of single-layer $CrTe_3$

Cite as: J. Appl. Phys. **127**, 033903 (2020); doi: 10.1063/1.5126246
Submitted: 31 August 2019 · Accepted: 4 January 2020 ·
Published Online: 17 January 2020

View Online Export Citation CrossMark

Zhi-Wei Lu,[1] Shao-Bin Qiu,[1] Wen-Qiang Xie,[1] Xiao-Bao Yang,[1,2] and Yu-Jun Zhao[1,2,a)]

AFFILIATIONS

[1]Department of Physics, South China University of Technology, Guangzhou 510640, China
[2]Key Laboratory of Advanced Energy Storage Materials of Guangdong Province, South China University of Technology, Guangzhou, Guangdong 510640, China

[a)]**Author to whom correspondence should be addressed:** zhaoyj@scut.edu.cn. **Tel.:** +86-20-87110426. **Fax:** +86-20-87112837

ABSTRACT

Developing novel controllable two-dimensional semiconductor materials is crucial to thin film spintronic devices, which may lead to a revolution of information devices. Recently, the easily cleavable $CrTe_3$ has attracted much attention for studying the magnetic properties of two-dimensional materials. In this paper, we have demonstrated theoretically that an elastic tensile strain can turn the antiferromagnetic coupled single-layer $CrTe_3$ (SL-$CrTe_3$) into a ferromagnetic (FM) system, favoring its potential application in thin film spintronic devices. The FM SL-$CrTe_3$ undergoes a further transition from a semiconductor to a metal under a biaxial tensile strain of 9%. The kinetic stability of SL-$CrTe_3$ under 10% tensile strain is verified by a molecular dynamics simulation at room temperature. We suppose that the strain-dependent magnetic behaviors of SL-$CrTe_3$ resulted from the competition between superexchange and direct interactions. The tunable magnetic and electronic properties of SL-$CrTe_3$ imply immense potential in spintronic device applications.

I. INTRODUCTION

The rapidly developing monolayer transition metal compounds have wide prospects in the application of ferromagnetic (FM) semiconductor based ultrathin spintronic devices, which can promote both device integration and performance.[1] MoS_2 and some other nanosheets have been successfully processed into high-performance transistors, which can be used for the construction of logic gate circuits.[2] Particularly, a flurry of research studies have been conducted in two-dimensional (2D) ferromagnetic coupling semiconductors with high Curie temperature (T_C) lately for thin film spintronic devices.[3] For instance, monolayer CrI_3 was found to be FM with out-of-plane spin orientation and a Curie temperature of 45 K.[4] The FM coupling in few-layer $Cr_2Ge_2Te_6$ can be enhanced experimentally by a small electric field.[5] Recently, obtaining 2D intrinsic FM semiconductor from antiferromagnetically coupled systems was proposed theoretically, including the monolayer CrOCl and CrOBr with a predicted T_C of 160 K and 129 K,[6] respectively. Nevertheless, their Curie temperatures are still too low for practical applications in spintronic devices, and exploring 2D intrinsic ferromagnetic semiconductors at room temperature is still challenging.

While intrinsic[7] and extrinsic defect[8] doping and charge doping[9] are often adopted to tune the magnetic property of various compounds, strain is a convenient and efficient approach to tune 2D films, as the magnetic properties of CrI_3[9] and $CrSiTe_3$[10] are shown theoretically to vary significantly under strain. It is lately reported that the FM coupling of monolayer materials like CrI_3 and $CrGeTe_3$ can be enhanced through reducing their virtual exchange gap (G_{ex}),[11] demonstrating that constructing alloyed transition metal compounds like $CrWI_6$ and $CrWGe_2Te_6$ can be a feasible way to reduce the G_{ex} of CrI_3 and $CrGeTe_3$, respectively. In addition, appropriate strain can also reduce the G_{ex} of these alloys.[11] Recently, $CrTe_3$, a layer stacking bulk with antiferromagnetic (AFM) coupling, was studied experimentally. With its cleavage energy as low as 0.5 J/m^2, very close to graphite, $CrTe_3$ is demonstrated to be easily cleavable from bulk-like graphene.[12]

Here, we find theoretically that the antiferromagnetically coupled $CrTe_3$ monolayer can be easily tuned into FM semiconductors by strain. Both FM stability and magnetic moment of atoms in single-layer $CrTe_3$ (SL-$CrTe_3$) can be enhanced obviously by applying biaxial tensile strain, whereas the AFM coupling can be strengthened with compression strain, with the magnetic properties

dominated by the competition between superexchange and direct interactions. SL-$CrTe_3$ also shows a semiconductor to metal transition under 9% tensile strain. These useful strain induced properties of SL-$CrTe_3$ provide great potential for spintronic device applications.

II. COMPUTATIONAL DETAILS

All calculations are based on spin-polarized density functional theory (DFT), implemented in the Vienna *ab initio* Simulation Package (VASP) code.[13,14] The Perdew–Burke–Ernzerhof (PBE) exchange-correlation functional[15] and the projector augmented wave (PAW) method[14] are used. Pseudopotentials with $3d^5 4s^1$ and $5s^2 5p^4$ valence electron configurations for Cr and Te atoms are adopted, respectively. A plane wave energy cutoff of 500 eV was employed for the basis set, while the Brillouin zone is represented by a set of $7 \times 7 \times 1$ k-points for the structural relaxation and by a $15 \times 15 \times 1$ mesh for electronic property calculations following the Monkhorst–Pack scheme.[16] The atomic structures are relaxed until the force reaches to less than 0.01 eV $Å^{-1}$. In the model of monolayer $CrTe_3$, a 20 Å thick vacuum region is added in the supercell to minimize the interaction between the periodic images. Monte Carlo (MC) simulations[17] for the magnetic phase transition of SL-$CrTe_3$ is performed by using the Vampire code.[18–20]

III. RESULTS AND DISCUSSION

A. Structure of bulk and monolayer $CrTe_3$

The model of bulk $CrTe_3$ is shown in Fig. 1(a). It crystallizes in the monoclinic structure with the space group P2/m,[21] containing numbers of lozenge shaped Cr_4 tetramers. Cr atoms are bonded by edge sharing octahedra of Te atoms. It is a layer stacking antiferromagnetically crystalline whose interlayer binding is dominated by van der Waals interactions. Therefore, its monolayer structure can be fabricated experimentally by some conventional methods, such as mechanical exfoliation.[22] The unit cell of bulk $CrTe_3$ contains eight formula units that consist of a Te–Cr–Te sandwiched structure. Our calculated value of its bandgap is 0.29 eV, which agrees well with its experimental value of 0.3 eV, although most of the PBE calculations underestimate the bandgaps.[12] As listed in Table I, the calculated lattice parameter of bulk $CrTe_3$ has been compared with experimental measurement,[12] where the *c*-axis length is clearly overestimated by about 7.2% compared to the experiment since the calculation neglects the long-range van der Waals interaction.[12] Meanwhile, the calculated *a* and *b* are in line with the experiment, within 0.5%–1.6%

TABLE I. The experimental and calculated lattice and structural parameters of bulk $CrTe_3$ and SL-$CrTe_3$. Data for SL-$CrTe_3$ are from its optimized ideal structure under AFM ground state.

	Source	*a* (Å)	*b* (Å)	*c* (Å)	$d_{Cr\text{-}Te}$ (Å)	$d_{Cr\text{-}Cr}$ (Å)
Bulk/Expt.	12	11.52	11.08	7.88	…	…
Bulk/Calc.	12	11.65	11.49	8.20	…	…
Bulk/Calc.	This work	11.58	11.26	8.45	2.73	3.70
Monolayer/Calc.	This work	11.55	11.09	…	2.73	3.64

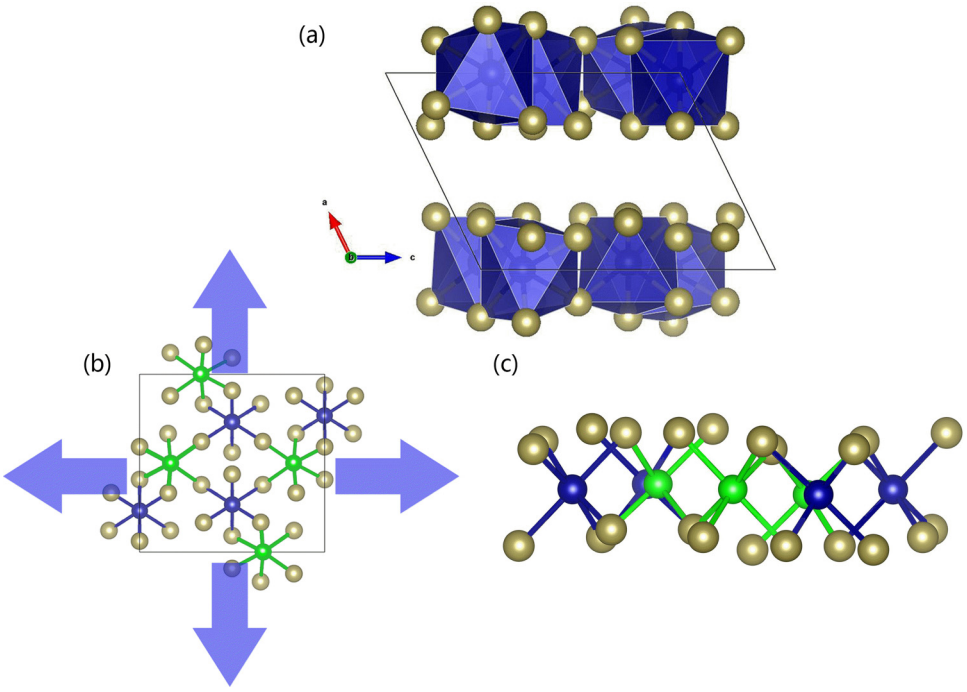

FIG. 1. (a) The crystal structure of bulk $CrTe_3$. (b) Top view and (c) side view of SL-$CrTe_3$, where the green and blue atoms represent two groups of nonequivalent chromium atoms Cr_1 and Cr_2, respectively. In addition, the green and blue lines represent the bond from two groups of Cr atoms (d_1 and d_2) to their adjoining six Te atoms, respectively.

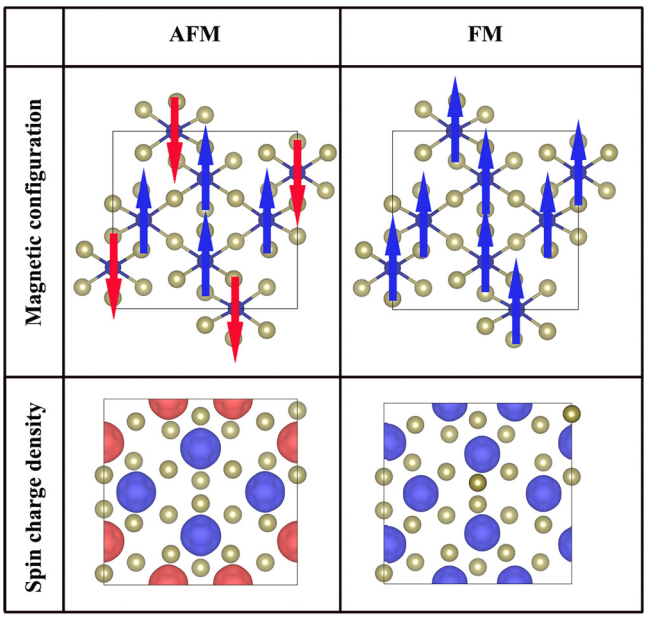

FIG. 2. AFM and FM configurations are shown. In addition, the spin charge density of AFM and FM are shown where blue and red isosurfaces correspond to spin-up and spin-down charge density, respectively.

difference, and also in good agreement with the available DFT calculations.[12]

The structural parameters (lattice constant and Cr–Te bond length) and the model of optimized SL-$CrTe_3$ without strain are listed in Table I and shown in Figs. 1(b) and 1(c), respectively. Based on the symmetry analysis, it is found that there are two groups of nonequivalent chromium atoms in the SL-$CrTe_3$ system, as shown in Fig. 1(b).

Our DFT calculation shows that 2D Young's modulus of SL-$CrTe_3$ along the a and b directions are 52 GPa nm and 48 GPa nm, respectively, which are greater than SL-CrI_3[9] but much smaller than graphene.[23] This suggests that the SL-$CrTe_3$ is much more flexible than graphene, and it can be sustained under a large strain range.[9]

B. Effect of strain on magnetic properties of SL-$CrTe_3$

We have studied the variation of spin order in SL-$CrTe_3$ and the energy difference between the AFM and FM states in SL-$CrTe_3$ (E_{AFM-FM}) under strain. All possible magnetic configurations of the SL-$CrTe_3$ unit cell are investigated, and the FM and energetically favored AFM configurations are shown in Fig. 2. The total energy changes under strain for AFM and FM states are also illustrated in Fig. 3(a). It is demonstrated that E_{AFM-FM} of SL-$CrTe_3$ increases monotonically with the increase of biaxial tensile strain and the FM state becomes more stable as shown in Fig. 3(a). In addition, FM coupling will be weakened and AFM becomes more stable under compression strain.

For convenience, we define the isotropic strain as $\varepsilon = \Delta c/c_0 \times 100\%$, where $c = c_0 + \Delta c$ and c_0 are the lattice constants with and without strain, respectively, as well as $\varepsilon > 0$ and $\varepsilon < 0$ stand for tensile and compression strains accordingly. At $\varepsilon = 0$, E_{AFM-FM} turns out to be negative, meaning AFM is the ground state of SL-$CrTe_3$ without strain. As the strain increases to $\varepsilon = 4\%$, E_{AFM-FM} turns to be positive and FM is favored, followed by a magnetic transition FM state that dominates significantly, and correspondingly, the energy difference between AFM and FM coupling is enhanced up to 82.1 meV/formula. Interestingly, E_{AFM-FM} decreases to -154 meV/formula at $\varepsilon = -4\%$, implying that AFM coupling will be strengthened significantly under compression strain.

Through spin-polarized calculation, it is found that the average magnetic moments of Cr atoms (M_{Cr}) and Te atoms (M_{Te}) in an ideal AFM state of SL-$CrTe_3$ are equal to 2.86 μ_B and 0.05 μ_B, respectively. From Fig. 2, we can see that the spin density locates

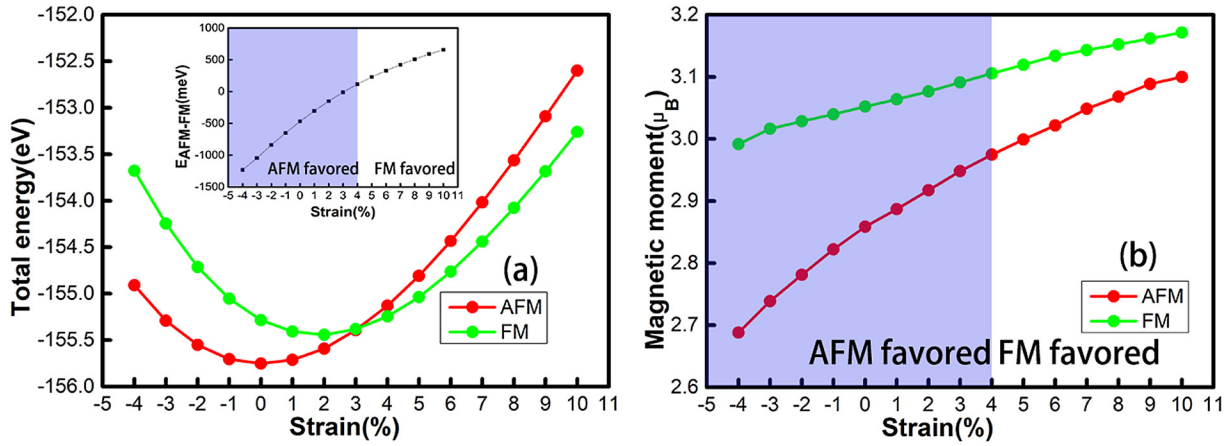

FIG. 3. Strain dependence of (a) total energy variation at AFM and FM states, and the inset shows the energy difference between AFM and FM coupling in SL-$CrTe_3$; (b) the average magnetic moments of Cr atoms in FM (green) and AFM (red) states.

mostly in Cr atoms, from which the magnetic moments of Te atoms are induced.

The average magnetic moments of Cr atoms, M_{Cr}, under various strains at AFM and FM states are illustrated in Fig. 3(b). M_{Cr} increases monotonically with the increase of tensile strain both at AFM and FM states and decreases rapidly under compression strain. At $\varepsilon = 10\%$, M_{Cr} increases up to 3.17 μ_B at the FM ground state. Yet, M_{Cr} decreases to 2.69 μ_B at $\varepsilon = -4\%$. It is understandable that the local magnetic moment can be enhanced through tensile strain and quenched under compression strain.

It is well known that magnetocrystalline anisotropy is required to stabilize long-range ferromagnetic ordering in 2D systems following the Mermin–Wagner theorem, as verified in monolayer CrI_3 with a Curie temperature of 45 K.[4] Based on the DFT calculations on the strain-dependent lattice structures, the strain induced change of magnetocrystalline anisotropy energy (MAE) of SL-$CrTe_3$ has been studied, which originates from the spin-orbital coupling (SOC) effects, establishing a long-range ferromagnetic ordering in SL-$CrTe_3$ at finite temperatures.[24] The total MAE is obtained as the total energy difference between E_{in} and E_{out}, where E_{in} and E_{out} are the energies when the spins of all chromium atoms are aligned along the in-plane and out-of-plane directions, respectively.[25] As shown in Fig. 4, the MAE is very small, ranging from −1 to 0.3 meV per unit cell under stains. This indicates that it is difficult for SL-$CrTe_3$ to counterbalance the thermal fluctuations, which implies its low Curie temperature.

To uncover the strain effect on the magnetic properties, the structural variation of SL-$CrTe_3$ along with strains has been studied. Based on the different behaviors of Cr–Cr and Cr–Te bond lengths responding to strains, the mechanism of magnetic transition can be explained by the theory of competition between superexchange and direct exchange interactions, in line with other two-dimensional materials such as VX_2 (X = S, Se)[26] NbX_2 (X = S, Se),[27] and $CrSiTe_3$.[10]

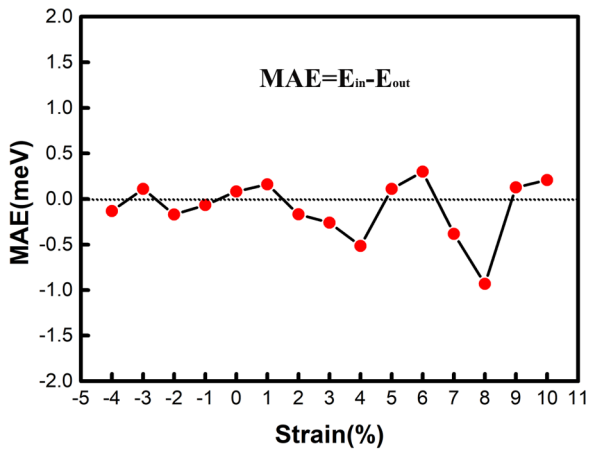

FIG. 4. The calculated strain-dependent magnetocrystalline anisotropy energy of $CrTe_3$ monolayer.

As shown in Fig. 5(c), the distance between a Cr atom and its neighbor Cr atom ($d_{Cr\text{-}Cr}$) increases rapidly. For the AFM (FM) state, $d_{Cr\text{-}Cr}$ increases from 3.29 Å (3.51 Å) under 4% compression strain to 4.16 Å (4.17 Å) under 10% tensile strain, by 26.4% (24.1%). The sensitive variation of $d_{Cr\text{-}Cr}$ implies that SL-$CrTe_3$ is a soft material, in line with the calculated low Young's modulus. As for the bond length of Cr–Te ($d_{Cr\text{-}Te}$) shown in Figs. 5(a) and 5(b), it varies much less than $d_{Cr\text{-}Cr}$ with strain. For AFM (FM) state, $d_{Cr\text{-}Te}$ varies to 2.69 Å (2.71 Å) of −4% strain from 2.81 Å (2.80 Å) under no strain, changing only by 4.5% (3.3%). This is related to the Cr–Te–Cr sandwiched structure, as the Cr–Cr distance varies in the same plane while Te atoms come closer to the Cr atom plane. The AFM coupling originates from the direct interaction of Cr and its neighbor Cr atoms, and the FM coupling originates from the superexchange interaction through Cr–Te–Cr bonding, which is sensitive to $d_{Cr\text{-}Cr}$ and $d_{Cr\text{-}Te}$, respectively. As discussed above, $d_{Cr\text{-}Cr}$ elongates much faster than $d_{Cr\text{-}Te}$ along with an increasing strain from −4% to 10%. Evidently, the direct interaction decays much faster than the superexchange interaction, leading to a rapid degrading of AFM coupling. On the other hand, the variation of the bond angle of Cr–Te–Cr along with strain is shown in Fig. 5(d). Dramatically, the Cr–Te–Cr bond angle turns to 89.96°, which is very close to 90° at the strain of 4%. This agrees well with the Goodenough–Kanamori–Anderson (GKA) rules,[28–30] which has explained the ferromagnetism of 1T-CrX_2 (X = Se, Te) monolayers well.[31] When Cr–Te–Cr bond angle reaches 90°, the electrons in the Te *p* state can easily excite to the Cr *d* state, which can enhance the high spin state and thus the FM coupling, as shown in Fig. 6. However, while the angle deviates from 90° and increases along with strain, the FM coupling is still more stable than AFM coupling. Why the FM coupling can decay slower than AFM coupling after the transition point? According to a recent research study, the superexchange FM coupling is closely related to the virtual exchange gap G_{ex} ($G_{ex} = E_{Cr\text{-}eg\uparrow} - E_{Cr\text{-}t2g\uparrow}$), as it is significant to enhance FM coupling through orbital engineering. The FM coupling of monolayer CrI_3 and $CrGeTe_3$ have been enhanced three to five times through forming alloy compounds, whose G_{ex} has been reduced significantly.[10]

It is known that the bandgap of $CrTe_3$ originates from the octahedral crystal field splitting t_{2g} and e_g orbitals, indicating that the bandgap $E_g \approx G_{ex}$. As shown in Fig. 7, E_g decreases after the transition to the FM state at 4% strain. So it is supposed that G_{ex} decreases along with the increase of biaxial tensile strain, similar to the G_{ex} variation of $CrWGe_2Te_6$ under tensile strain,[11] which results in the enhancement of FM coupling. Therefore, the decrease of G_{ex} has a significant contribution to slow down the weakening of FM coupling, along with the fast degrading of AFM coupling owing to the increase of $d_{Cr\text{-}Cr}$. It is significantly shown that the distance between two groups of nonequivalent Cr atoms and their adjacent Te atoms have the same value in the transition point 4%. After the magnetic transition, d_1 is greater than d_2. We suppose that it is related to the different G_{ex} in two groups of Cr atoms, which may be a complicated competition. To this end, it is indicated that the slower decay of FM coupling along with biaxial tensile strain can be explained by the GKA rule and decrease of G_{ex}.

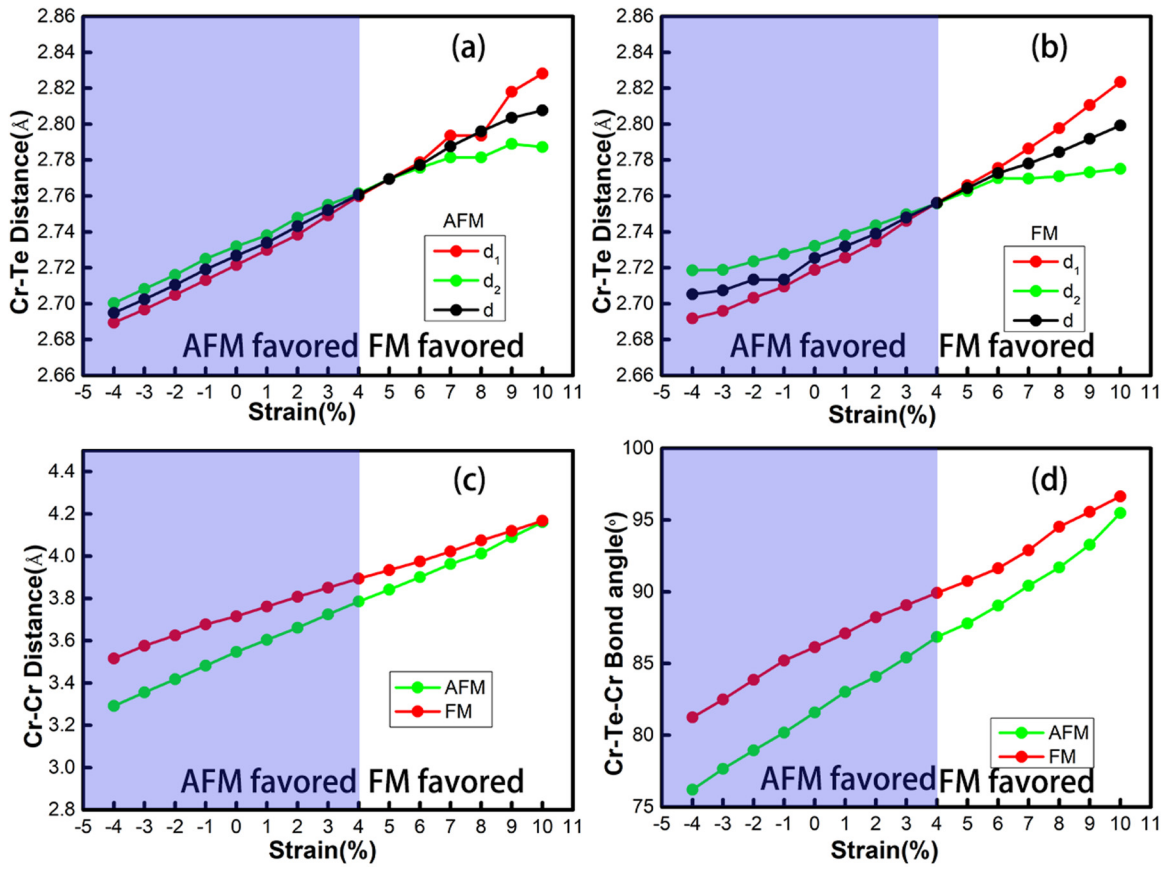

FIG. 5. The average distance between the two groups of nonequivalent Cr atoms (d_1 and d_2), and the average distance of all chromium atoms and their adjacent Te atoms at AFM (a) and FM (b) phases, respectively. The Cr–Cr bond length and Cr–Te–Cr bond angle are shown in (c) and (d), respectively.

C. Effect of strain on electronic properties of SL-$CrTe_3$

In order to further understand these strain-dependent magnetic behaviors, the density of states (DOS) and projected density of states (PDOS) of the AFM ground state SL-$CrTe_3$ are plotted in Fig. 8. From the band structure, we find that the valence band maximum (VBM) and conduction band minimum (CBM) of the strain free SL-$CrTe_3$ locate at different points in the line of Γ to Y, presenting semiconductor characteristics with an indirect gap of 0.42 eV. It is shown that the VBM and CBM are mainly contributed by Cr *d* states and Te *p* states, respectively.

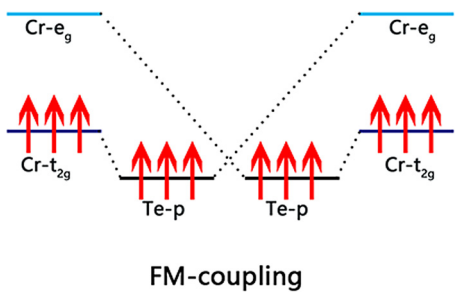

FIG. 6. Schematic diagrams of FM coupling in the $CrTe_3$ monolayer, which is similar to $CrGeTe_3$.[11]

Furthermore, Cr and Te atoms in system form Cr–Te covalent-like bonds. As a result, electrons are bound in these states and the carrier mobility is low in SL-$CrTe_3$, where the flatbands near the Fermi level verify it. It is generally known that the *d* orbital of Cr atoms split into t_{2g} and e_g orbitals in the $CrTe_6$ octahedron, which is the origin of bandgap in SL-$CrTe_3$. Normally in the SL-$CrTe_3$ octahedral crystal field, the lower threefold t_{2g} orbitals are occupied by three electrons with the same spin while the higher twofold e_g orbital is empty, exhibiting a high spin state. However, the situation becomes more complicated since the electrons in *p* orbitals of Te atoms will excite to Cr e_g orbitals when the Cr–Te–Cr bond angle is close to 90° according to GKA rules, making e_g orbitals non-degenerate, enhancing the Jahn–Teller effect.[32]

In addition to the transition of magnetic coupling, the electronic properties vary with strain sensitively. As shown in Fig. 7, the bandgap of spin-up and spin-down channels varying with

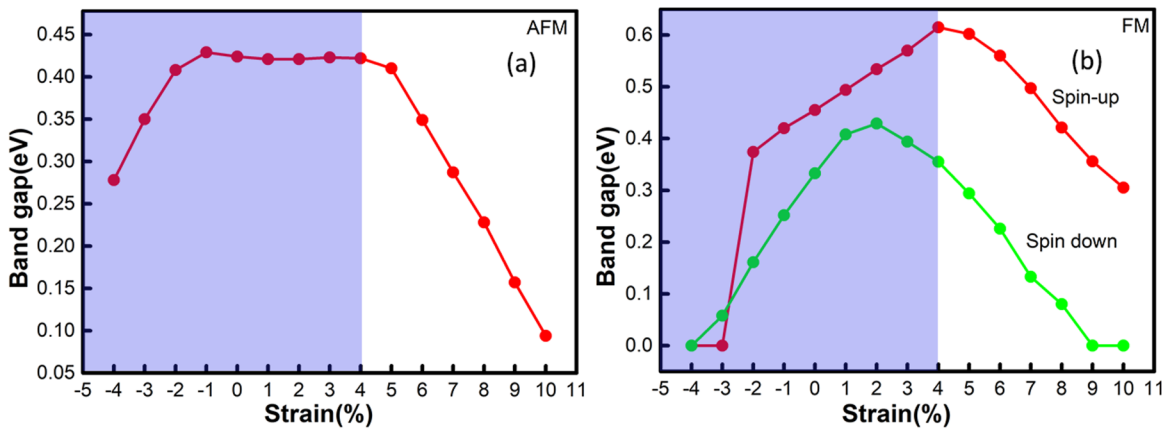

FIG. 7. The bandgaps of up and down spins vary with the strain at AFM (a) and FM (b) states. The shadowed and non-shadowed areas indicate the situation before and after magnetic transition, respectively.

strain are shown in AFM and FM states, respectively. The FM state is more sensitive than AFM before the magnetic transition point of 4%, and it is in contrast after the magnetic transition point. Under the range of 4%–8% in the FM state, both spin-up and spin-down channels open a gap, showing a semiconductor character. While under 9% tensile strain, SL-$CrTe_3$ exhibits metal characteristics. In order to understand the mechanism of semiconductor to metal transition induced by biaxial tensile strain, the projected density of states (PDOS) of SL-$CrTe_3$ has been exhibited in Fig. 9. For the tensile strain of 4%, the Te p_y orbital is enhanced and both spin-up Cr t_{2g} and e_g as well as Te p_y orbitals locate at the VBM, exhibiting a semiconductor character. When strain reaches to 9%, the spin-down Te p_z orbital goes downward the VBM and spin-up Cr t_{2g} and e_g orbitals shift away from the VBM, while the spin-up Te p_y orbital still shows a large contribution at the VBM, exhibiting a metal character. It is clear that the semiconductor to metal transition of SL-$CrTe_3$ is owing to the variation of dominated Cr *d* and Te *p* components.

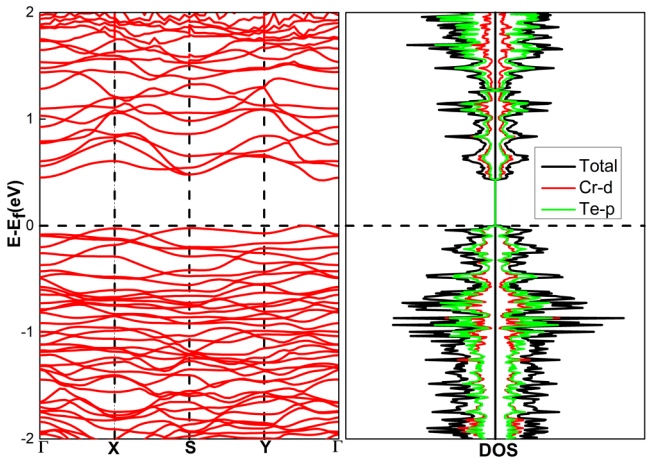

FIG. 8. Band structure, total DOS, and PDOS of AFM SL-$CrTe_3$, with the Fermi level set to zero.

D. Structural stability of strained systems

In order to examine its kinetic stability at room temperature, a canonical ensemble is performed using the algorithm of Nosé[33] by

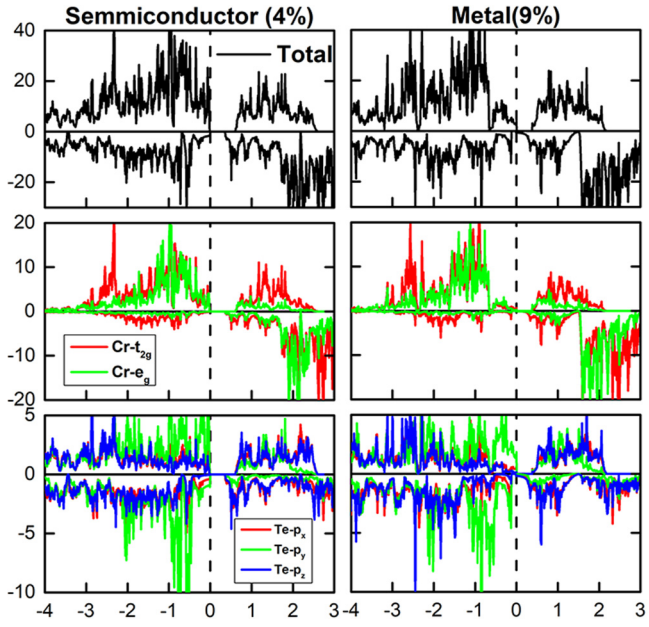

FIG. 9. The projected density of states of *FM* SL-$CrTe_3$ under various strains.

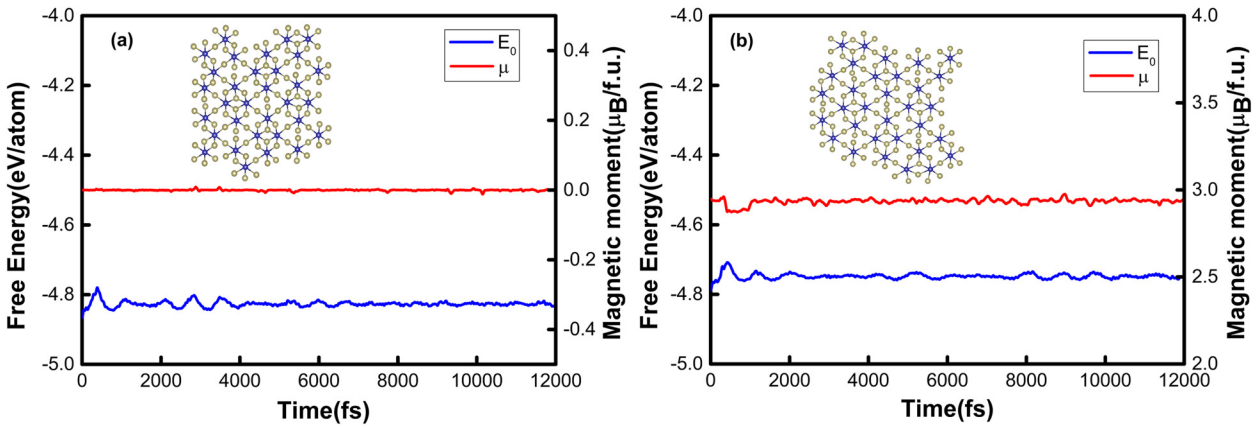

FIG. 10. Variations of free energy and magnetic moment of SL-$CrTe_3$ under the situation without strain (a) and with 10% biaxial tensile strain (b), performing *ab initio* molecular dynamics simulation at a temperature of 300 K. The insets show the atomic configuration at t = 12 ps, correspondingly.

ab initio molecular dynamics (AIMD) simulations.[34] A 128-atom 2D structure was simulated by AIMD at a temperature of 300 K for 12 ps. As shown in Figs. 10(a) and 10(b), free energy of this 2D network under the situation of both strain free and 10% biaxial tensile strain converge to a stable level, and the structure under both situations are maintained well with a small distortion within 12 ps, indicating that the SL-$CrTe_3$is kinetically stable without structural destruction in both situations. In addition, the magnetic moment of both structures shows a small fluctuation around 0 and 3.0 μ_B, suggesting that AFM coupling is stable at no strain, while FM is stable under 10% tensile strain at room temperature, respectively.

In order to understand the behavior of magnetism with temperature, the Curie temperature has been estimated by Monte Carlo (MC) simulations.[17] We have studied the magnetic moment of one formula unit cell at different temperatures. The classical 3D Heisenberg spin Hamiltonian[20,25] is defined as

$$H = -\frac{1}{2}\sum_{i,j} J_{ij} S_i \cdot S_j - \sum_i k_u S_{i,z}^2 - \mu_S \sum_i B \cdot S_i. \quad (1)$$

In this model, J_{ij} is the Heisenberg isotropic exchange parameter considering third neighbor magnetic interaction. S_i and S_j represent the magnetic moments of the two neighbor atoms. k_u is the anisotropic parameter and μ_S is the magnetic moment of the chromium atom. B is the external magnetic field, which is set to zero in this work. The strength of the anisotropy is determined by k_u, where positive and negative values indicate the alignment along out-of-plane and in-plane, respectively. The anisotropic parameter k_u is equal to the anisotropy energy.[18]

In the MC simulations, a 50×50 supercell has been adopted, where 2×10^5 loops are taken to achieve equilibrium and 10^5 loops are taken to collect the average of magnetic moment. The three magnetic exchange parameters are regressed from the DFT energy calculations of all nonequivalent magnetic configurations in SL-$CrTe_3$ unit cell of 32 atoms, as listed in Table II. The value of k_u is rather small ranged from −1 to 0.3 meV as strain changes. In Fig. 11(a), its Curie temperature is estimated to be 7 K with 4% biaxial tensile strain and it can be enhanced to 9 K when the tensile strain increases to 10%. A Monte Carlo (MC) simulation based on the 2D Ising model[20] is conducted for comparison [cf. Fig. 11(b)]:

$$H = -\frac{1}{2}\sum_{i,j} J_{ij} S_i \cdot S_j. \quad (2)$$

The magnetic moment drops around 15 K from 3.0 μ_B to zero in the case of 4% biaxial tensile strain. Interestingly, T_C can be enhanced to 25 K when the tensile strain increases to 10%. From Figs. 11(a) and 11(b), we can see a large reduction of Curie temperature in the 3D Heisenberg Monte Carlo simulations when the magnetocrystalline anisotropy is included. It is more reasonable to include the magnetocrystalline anisotropy effect, as it is necessary to eliminate the Mermin–Wagner limit in 2D materials.[4] The T_C obtained by mean-field approximation (MFA)[35] is 33 K and 81 K under 4% and 10% biaxial tensile strain, respectively. It is known that the Monte Carlo simulation is more accurate for T_C estimation and generally has a lower estimated T_C than that of MFA. Even though its Curie temperature is still low, it may be further improved by the substrate or doping. The Néel temperature (T_N) of the strain free SL-$CrTe_3$ is also estimated by 3D Heisenberg and 2D

TABLE II. The magnetic exchange parameters up to third neighbors and anisotropic parameters under strain free and 4% and 10% biaxial tensile strains.

	J_1 (meV)	J_2 (meV)	J_3 (meV)	k_u (μeV)
Strain 0%	−3.63	−8.03	0.89	9.28
Strain 4%	0.87	1.73	0.38	−57.29
Strain 10%	2.46	5.28	−0.17	23.05

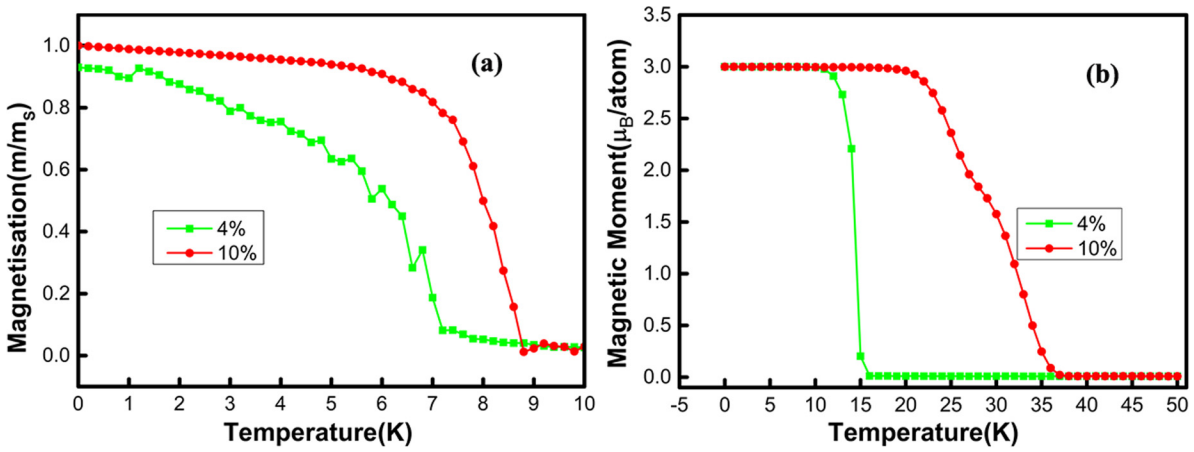

FIG. 11. Variation of the mean magnetic moment per Cr atom of SL-$CrTe_3$ with respect to the temperature under the strain of 4% and 10%, calculated by 3D Heisenberg (a) and 2D Ising model (b) Monte Carlo simulations, respectively.

Ising model Monte Carlo simulations, which is 18 K and 30 K, respectively.

IV. CONCLUSION

In this paper, we have explored the strain-dependent magnetic and electronic properties of SL-$CrTe_3$. With the increase of biaxial strain, both the magnetic moment of Cr atoms and stability of the FM state are monotonically enhanced in SL-$CrTe_3$. The stability of the FM state gradually enhances and an AFM to FM phase transition occurs at the tensile strain of 4%. By contrast, the AFM state is more stable under compression strain. We have demonstrated that the variations of bond length and bond angle in the system are the major reason for the transition according to the GKA rules. The decrease of G_{ex} is responsible for the slower weakening of FM after the transition point. In addition, the FM SL-$CrTe_3$ further turns from a semiconductor to a metal under 9% biaxial tensile strain. Its Curie temperature can be enhanced with the increase of biaxial tensile strain, and its thermal stability at room temperature is verified. Its very small exchange parameter and MAE imply the weak magnetic interaction and stability, which agree well with our predicted low Curie temperature or Néel temperature. Our calculation indicates that the SL-$CrTe_3$ has a remarkable magnetic controllability under strain, earning it consideration as a suitable candidate for low-dimensional spintronic devices.

ACKNOWLEDGMENTS

This work was financially supported by the National Science Foundation of China (NSFC) (Grant Nos. 11574088 and 51431001), the Foundation for Innovative Research Groups of the National Natural Science Foundation of China (Grant No. 51621001), and the Natural Science Foundation of Guangdong Province of China (Grant No. 2016A030312011). The computer times at the National Supercomputing Center in Guangzhou (NSCCGZ) and Guangzhou Ginpie Technology are gratefully acknowledged.

REFERENCES

[1]C. Tan, X. Cao, X. J. Wu, Q. He, J. Yang, X. Zhang, J. Chen, W. Zhao, S. Han, and G. H. Nam, Chem. Rev. **117**, 6225 (2017).
[2]Z. Lin, Y. Liu, U. Halim, M. Ding, Y. Liu, Y. Wang, C. Jia, P. Chen, X. Duan, C. Wang, F. Song, M. Li, C. Wan, Y. Huang, and X. Duan, Nature **562**, 254–258 (2018).
[3]Z. Wang, T. Zhang, M. Ding, B. Dong, Y. Li, M. Chen, X. Li, J. Huang, H. Wang, X. Zhao, Y. Li, D. Li, C. Jia, L. Sun, H. Guo, Y. Ye, D. Sun, Y. Chen, T. Yang, J. Zhang, S. Ono, Z. Han, and Z. Zhang, Nat. Nanotechnol. **13**, 554–559 (2018).
[4]B. Huang, G. Clark, E. N. Navarro-Moratalla, D. R. Klein, R. Cheng, K. L. Seyler, D. Zhong, E. Schmidgall, M. A. McGuire, D. H. Cobden, W. Yao, D. Xiao, P. Jarillo-Herrero, and X. Xu, Nature **546**, 270 (2017).
[5]C. Gong, L. Li, Z. Li, H. Ji, A. Stern, Y. Xia, T. Cao, W. Bao, C. Wang, Y. Wang, Z. Q. Qiu, R. J. Cava, S. G. Louie, J. Xia, and X. Zhang, Nature **546**, 265 (2017).
[6]N. Miao, B. Xu, L. Zhu, J. Zhou, and Z. Sun, J. Am. Chem. Soc. **140**, 2417–2420 (2018).
[7]H. Cheng, J. Zhou, M. Yang, L. Shen, J. Linghu, Q. Wu, P. Qian, and Y. P. Feng, J. Mater. Chem. C **6**, 8435–8443 (2018).
[8]B. Xia, Q. Guo, D. Gao, S. Shi, and K. Tao, J. Phys. D Appl. Phys. **49**, 165003 (2016).
[9]F. Zheng, J. Zhao, Z. Liu, M. Li, M. Zhou, S. Zhang, P. Zhang, F. Zheng, J. Zhao, and Z. Liu, Nanoscale **10**, 14298 (2018).
[10]X. Chen, J. Qi, and D. Shi, Phys. Lett. A **379**, 60–63 (2015).
[11]C. Huang, J. Feng, F. Wu, D. Ahmed, B. Huang, H. Xiang, K. Deng, and E. Kan, J. Am. Chem. Soc. **140**, 11519–11525 (2018).
[12]M. A. Mcguire, V. O. Garlea, K. C. Santosh, V. R. Cooper, J. Yan, H. Cao, and B. C. Sales, Phys. Rev. B. **95**, 144421 (2017).
[13]G. Kresse and J. Furthmuller, Phys. Rev. B **54**, 11169 (1996).
[14]G. Kresse and D. Joubert, Phys. Rev. B **59**, 1758 (1999).
[15]J. P. Perdew, K. Burke, and M. Ernzerhof, Phys. Rev. Lett. **77**, 3865–3868 (1996).
[16]H. J. Monkhorst and J. D. Pack, Phys. Rev. B **13**, 5188–5192 (1976).
[17]D. A. Garanin, Phys. Rev. B **53**, 11593–11605 (1996).

[18]R. F. L. Evans, W. J. Fan, P. Chureemart, T. A. Ostler, M. O. A. Ellis, and R. W. Chantrell, J. Phys. Condens. Matter **26**, 103202 (2014).
[19]P. Asselin, R. F. L. Evans, J. Barker, R. W. Chantrell, R. Yanes, O. Chubykalo-Fesenko, D. Hinzke, and U. Nowak, Phys. Rev. B **82**, 054415 (2010).
[20]R. F. L. Evans, U. Atxitia, and R. W. Chantrell, Phys. Rev. B **91**, 144425 (2015).
[21]K. O. Klepp and H. Ipser, Monatsh. Chem. **110**, 499 (1979).
[22]L. Hai, W. Jumiati, Y. Zongyou, and Z. Hua, Acc. Chem. Res. **47**, 1067–1075 (2014).
[23]C. Lee, X. Wei, J. W. Kysar, and J. Hone, Science **321**, 385 (2008).
[24]J. Lado and J. Fernández-Rossier, 2D Mater. **4**, 035002 (2017).
[25]J. Liu, M. Pinghui, S. Mengchao, G. Dan, and L. Jiwu, J. Appl. Phys. **124**, 044303 (2018).
[26]M. Yandong, D. Ying, G. Meng, N. Chengwang, Z. Yingtao, and H. Baibiao, ACS Nano **6**, 1695–1701 (2012).
[27]Y. Zhou, Z. Wang, P. Yang, X. Zu, L. Yang, X. Sun, and F. Gao, ACS Nano **6**, 9727–9736 (2012).
[28]J. B. Goodenough, Phys. Rev. **100**, 564–573 (1955).
[29]J. Kanamori, J. Appl. Phys. **31**, S14–S23 (1960).
[30]P. W. Anderson, Phys. Rev. **115**, 2–13 (1959).
[31]H. Y. Lv, W. J. Lu, D. F. Shao, Y. Liu, and Y. P. Sun, Phys. Rev. B **92**, 214419 (2015).
[32]I. B. Bersuker, Chem. Rev. **113**, 1351–1390 (2013).
[33]S. Nosé, J. Chem. Phys. **81**, 511–519 (1984).
[34]D. Bucher, L. C. T. Pierce, J. A. McCammon, and P. R. L. Markwick, J. Chem. Theory. Comput. **7**, 890–897 (2011).
[35]S. Lv, H. Li, X. Liu, D. Han, Z. Wu, and J. Meng, J. Phys. Chem. C **114**, 16710–16715 (2010).